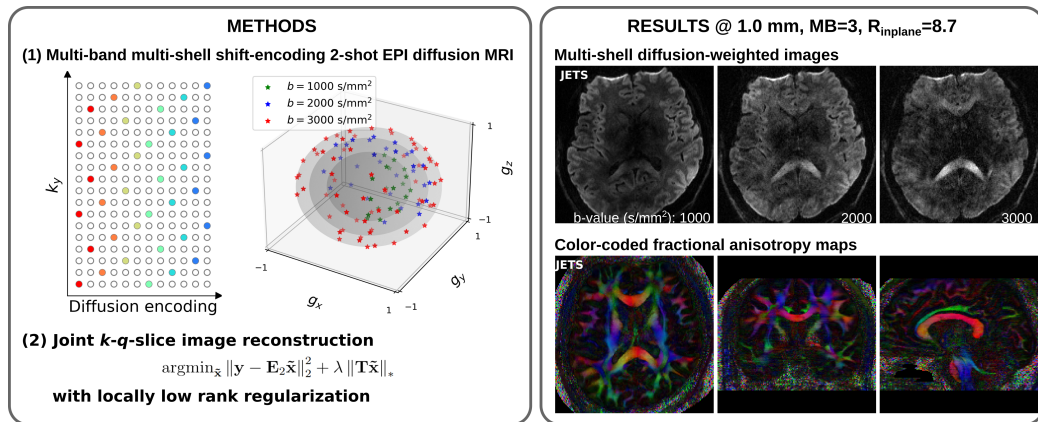


Graphical Abstract

Accelerated Diffusion Weighted Magnetic Resonance Imaging at 7 T: Joint Reconstruction for Multi-Shell Multi-Band Shift-Encoded Echo Planar Imaging (JETS-EPI)

Zhengguo Tan, Patrick Alexander Liebig, Robin Martin Heidemann, Frederik Bernd Laun, Florian Knoll



Highlights

Accelerated Diffusion Weighted Magnetic Resonance Imaging at 7 T: Joint Reconstruction for Multi-Shell Multi-Band Shift-Encoded Echo Planar Imaging (JETS-EPI)

Zhengguo Tan, Patrick Alexander Liebig, Robin Martin Heidemann, Frederik Bernd Laun, Florian Knoll

- Novel accelerated diffusion acquisition with shifted phase encoding among diffusion directions for complementary k - q -space sampling at 7 T
- Generalized joint k - q -slice diffusion-weighted image reconstruction with overlapping locally low-rank regularization
- 5 min 1.2 mm isotropic resolution with b -value 1000 s/mm^2 and 32 diffusion directions for in vivo whole-brain diffusion tensor imaging
- 23 min 1 mm isotropic resolution with three-shell high b -values (up to 3000 s/mm^2) and 126 diffusion directions for in vivo whole-brain diffusion tensor imaging and fiber orientation distribution function (fODF) mapping

Accelerated Diffusion Weighted Magnetic Resonance Imaging at 7 T: Joint Reconstruction for Multi-Shell Multi-Band Shift-Encoded Echo Planar Imaging (JETS-EPI)

Zhengguo Tan^a, Patrick Alexander Liebig^b, Robin Martin Heidemann^b,
Frederik Bernd Laun^c, Florian Knoll^a

^a*Department Artificial Intelligence in Biomedical Engineering
(AIBE), Friedrich-Alexander-Universität Erlangen-Nürnberg Erlangen, Germany*

^b*Siemens Healthcare GmbH, Erlangen, Germany*

^c*Institute of Radiology, University Hospital Erlangen Friedrich-Alexander-Universität Erlangen-Nürnberg Erlangen, Germany*

Abstract

The pursuit of high spatial-angular-temporal resolution for in vivo diffusion-weighted magnetic resonance imaging (DW-MRI) at ultra-high field strength (e.g., 7 T) is important in understanding brain microstructure and function. Such pursuit, however, faces several technical challenges. First, increased off-resonance and shorter T_2 relaxation require faster echo train readouts. Second, high angular resolution in q -space requires the use of high and/or multiple b -values. High b -values supply strongly diffusion-weighted images, which have lower signal-to-noise ratio (SNR). Multi-shot interleaved echo-planar imaging (EPI) and advanced reconstruction strategies have been proven suitable for high-resolution DW-MRI. These methods, however, utilize fully-sampled EPI and thus require longer scan time compared to single-shot EPI. To address these challenges, we developed the k_y shift encoding scheme among diffusion encodings to explore complementary k - q -space sam-

R3.13

R1.6

pling. Moreover, we developed a novel joint reconstruction with locally low rank regularization for multi-shell multi-band shift-encoding acquisition at 7 T (JETS-EPI). Our sampling method allows for faster acquisition with the use of high in-plane undersampling and only two shots per diffusion direction. The proposed joint reconstruction exhibits better denoising of DW images and clearer delineation of fiber distributions.

Keywords: Diffusion-weighted magnetic resonance imaging, Echo planar imaging, Ultra high field, Joint reconstruction, Low rank, Simultaneous multi slice

¹ **1. Introduction**

² Diffusion-weighted magnetic resonance imaging (DW-MRI) ([Le Bihan et al., 1986; Merboldt et al., 1985](#)) is a non-invasive modality that is sen-
³ sitive to Brownian motion of water molecules. DW-MRI forms the basis for
⁴ diffusion tensor imaging (DTI) ([Basser et al., 1994; Mori et al., 1999](#)) and
⁵ high angular resolution diffusion imaging (HARDI) ([Tuch et al., 2002](#)), and
⁶ has been widely used in acute brain ischemia diagnosis, in tumor detection
⁷ and staging, and in neuroscience ([Jones, 2010](#)).

⁹ For DW-MRI acquisition, the commonly used pulse sequence is single-
¹⁰ shot echo-planar imaging (SS-EPI) ([Mansfield, 1977](#)). SS-EPI is capable of
¹¹ rapidly acquiring one DW image per radio-frequency excitation at the order
¹² of 100 ms, and is thus motion robust. However, conventional SS-EPI, even
¹³ with three-fold accelerated acquisition ([Bammer et al., 2001](#)) using parallel
¹⁴ imaging ([Roemer et al., 1990; Ra and Rim, 1993; Pruessmann et al., 1999;](#)
¹⁵ [Griswold et al., 2002](#)), still suffers from low spatial resolution and geometric
¹⁶ distortions.

¹⁷ In the quest for high spatial-angular-temporal-resolution and minimal-ge- R3.7,
¹⁸ ometry-distortion DW-MRI, tremendous efforts have been made. Techniques R3.8
¹⁹ on the correction of image distortion induced by off-resonance and eddy
²⁰ currents have been developed ([Andersson et al., 2003](#)). Furthermore, gSlider
²¹ ([Setsompop et al., 2018](#)) with blipped-CAIPI ([Setsompop et al., 2012](#)) for si-
²² multaneous multi-slice (SMS) ([Maudsley, 1980; Breuer et al., 2005](#)) was pro-
²³ posed to achieve high-resolution DW-MRI. Advanced pulse sequences based
²⁴ on [multi-shot EPI](#) have also been developed, including but not limited to R3.15
²⁵ interleaved EPI ([Butts et al., 1993](#)), PROPELLER ([Pipe et al., 2002](#)), and

26 readout-segmented EPI (Porter and Heidemann, 2009; Heidemann et al.,
27 2010). Based on 4-shot interleaved EPI, advanced image reconstruction
28 techniques, e.g. multiplexed sensitivity encoding (MUSE) achieved DW-MRI
29 with sub-millimeter in-plane resolution and maximal b -value 2000 s/mm^2 at
30 3 T (Chen et al., 2013). In MUSE, four shots (i.e., four-fold undersampling
31 per shot) are used because of two reasons. First, the high spatial resolution
32 requires the use of multi-shot acquisition, which employs a shorter echo train
33 length per shot. This allows for reduced echo time and less spatial distortion.
34 Second, MUSE employs parallel imaging to reconstruct single-shot images for
35 the extraction of shot-to-shot phase variation, and four-fold undersampling
36 per shot is achievable in parallel imaging.

37 Multi-shot EPI, however, prolongs the acquisition time as well as intro- R3.8
38 duces motion sensitivity, i.e., shot-to-shot phase variation. Recently, com-
39 pressed sensing (Lustig et al., 2007; Block et al., 2007) has been explored to
40 accelerate multi-shot EPI acquisition. For instance, multi-shot reconstruc-
41 tion techniques based on structured low-rank matrix completion (MUSSELS)
42 (Mani et al., 2017; Bilgic et al., 2019) achieved 5-shot DW-MRI with 9-fold
43 undersampling per shot. Both MUSSELS and MUSE target the reconstruc-
44 tion of one DW image from interleaved EPI using at least 4 shots, i.e., joint-
45 k - q -space undersampling is not explored.

46 Joint- k - q -space undersampling can be achieved via proper regularization R1.2,
47 along the diffusion encoding direction. Relevant examples are diffusion un-
48 dersampling with Gaussian process estimated reconstruction (DAGER) (Wu
49 et al., 2019) and magnitude-based spatial-angular locally low-rank regular-
50 ization (SPA-LLR) (Hu et al., 2020). However, DAGER addresses the recon- R1.10

51 construction problem of single-shot EPI acquisition. SPA-LLR focuses on the
52 reconstruction of single-band and in-plane fully-sampled acquisition.

53 In this work, we propose a Joint k - q -slice rEconsTruction framework for
54 multi-band multi-shell Shift-encoded EPI at 7T (dubbed as JETS-EPI).

55 First, our acquisition method differs from most existing techniques as it shifts
56 the k -space in-plane sampling pattern along the phase encoding (k_y) direc-
57 tion. This shifting creates complementary k - q -space sampling. Second, our
58 reconstruction framework generalizes to jointly reconstruct multi-slice multi-
59 shell multi-direction DW images. This is built upon comprehensive modeling
60 of the acquisition process and construction of regularization terms (e.g. LLR)
61 as proximal operators. We compared our proposed method with state-of-the-
62 art multi-shot reconstruction techniques, i.e., MUSE and MUSSELS, as well
63 as an established local PCA-based DW image denoising algorithm, (Manjón R3.20
64 et al., 2013; Veraart et al., 2016). Our proposed method achieves 7T three-
65 shell high b -value (up to 3000 s/mm²) and 126 diffusion direction measure-
66 ments at 1 mm isotropic resolution in less than 23 min.

67 **2. Materials and methods**

68 *2.1. Multi-band multi-shell shift-encoded EPI acquisition*

69 Fig. 1 (A) displays diffusion weighted image acquisition based on two-shot
70 interleaved EPI. Conventionally, such a sampling pattern is repeated for all
71 diffusion directions. In contrast, we propose the k_y -shifted diffusion encod-
72 ing, as shown in Fig. 1 (B). The interleaved EPI sampling pattern is shifted
73 by one k_y line per diffusion direction, with the cycling period being the in-
74 plane undersampling factor. Fig. 1 (C) displays the employed multi-shell
75 sampling pattern. Every diffusion direction is distinct from others, thereby
76 constructing a non-collinear sampling pattern. This k_y -shifted non-collinear
77 diffusion encoding exploits complementary k - q -space sampling. Its proper-
78 ties are two-fold. First, the k_y -shifting is linear and retains consistent echo
79 spacing. Second, DW images share anatomical structures but differ in image
80 contrast depending on b -values and diffusion directions, thus complementary
81 q -space sampling is well suited for the exploration of structural similarity.

82 *2.2. In vivo acquisition protocols*

83 We implemented multiple in-vivo acquisition protocols at a clinical 7T
84 MR system (MAGNETOM Terra, Siemens Healthineers, Erlangen, Ger-
85 many) equipped with a 32-channel head coil (Nova Medical, Wilmington,
86 MA, USA) and the XR-gradient system (**maximum gradient strength 80 mT/m**
87 **with a peak slew rate of 200 T/m/s**). To calibrate coil sensitivity maps, refer- R3.22
88 ence scans employed a gradient-echo (GRE) sequence. Spectral fat saturation
89 and mono-polar diffusion-encoding gradients were used. The phase-encoding
90 direction was selected as anterior-to-posterior.

91 This study was approved by the local ethics committee. Three volunteers R3.1
92 with informed consent obtained before scanning participated in this study.
93 Detailed acquisition parameters are listed below.

94 *2.2.1. 20-diffusion-direction 6-shot acquisition at 1.0 mm³ isotropic resolu- R3.1
95 tion and b-value 1000 s/mm²*

96 This protocol employed 200 mm FOV in both read and phase-encoding
97 directions, base resolution 200, 141 slices, bandwidth 1086 Hz/Pixel, echo
98 spacing 1.06 ms, TE 59 ms, TR 7600 ms. Six shots per diffusion encoding with
99 partial Fourier 6/8 along the phase-encoding direction was used to acquire
100 in-plane full-sampled data. In other words, except partial Fourier, no in-
101 plane undersampling was used. Slice acceleration with a multi-band factor 3
102 was used.

103 The acquired data served as ground truth. We retrospectively reduced the R1.1
104 data to only two shots per diffusion encoding with and without the proposed
105 k_y shifting to simulate three-fold in-plane undersampling. JETS reconstruc-
106 tion was performed on all data to validate the proposed two-shot k_y -shifted
107 acquisition.

108 In addition, different reconstruction methods, i.e., JETS, MUSE, and R1.2
109 JULEP were performed on the six-shot data to validate the JETS recon-
110 struction quality.

111 *2.2.2. Single-shell diffusion acquisition at 1.2 mm³ isotropic resolution*

112 This protocol employed 220 mm FOV in both read and phase-encoding di- R1.11
113 rections, base resolution 182, 94 slices, bandwidth 1832 Hz/Pixel, echo spac-
114 ing 0.75 ms, TE 47 ms, TR 4300 ms, 2 shots per diffusion direction, in-plane

undersampling 3 as well as partial Fourier 6/8 along the phase-encoding direction, and multi-band factor 2. This results in 8.7×2 fold undersampling per shot. 30 diffusion directions with b -value 1000 s/mm^2 and 2 diffusion directions with b -value 50 s/mm^2 were acquired at a total scan time of **5.05 min.** Given the high spatial resolution and the short scan time, this protocol fits R3.24 well into clinical studies.

2.2.3. Three-shell diffusion acquisition at 1 mm^3 isotropic resolution

This protocol employed the same FOV, shots, in-plane undersampling, and partial Fourier as in Section 2.2.2. Other parameters were base resolution 214, 114 slices, bandwidth 1460 Hz/Pixel, echo spacing 0.81 ms, TE 66 ms, TR 5200 ms, and multi-band factor 3. This results in 8.7×3 fold undersampling per shot. As shown in Fig. 1 (C), three shells were sampled (1st shell: 20 diffusion directions with b -value 1000 s/mm^2 , 2nd shell: 30 diffusion directions with b -value 2000 s/mm^2 , and 3rd shell: 64 diffusion directions with b -value 3000 s/mm^2). b_0 acquisitions were interspersed every ten diffusion directions. This corresponds to a total of 126 DW acquisition volumes and **22.42 min** scan time. This protocol will be used to demonstrate the capabilities of JETS-EPI in achieving high spatial-angular-temporal resolution.

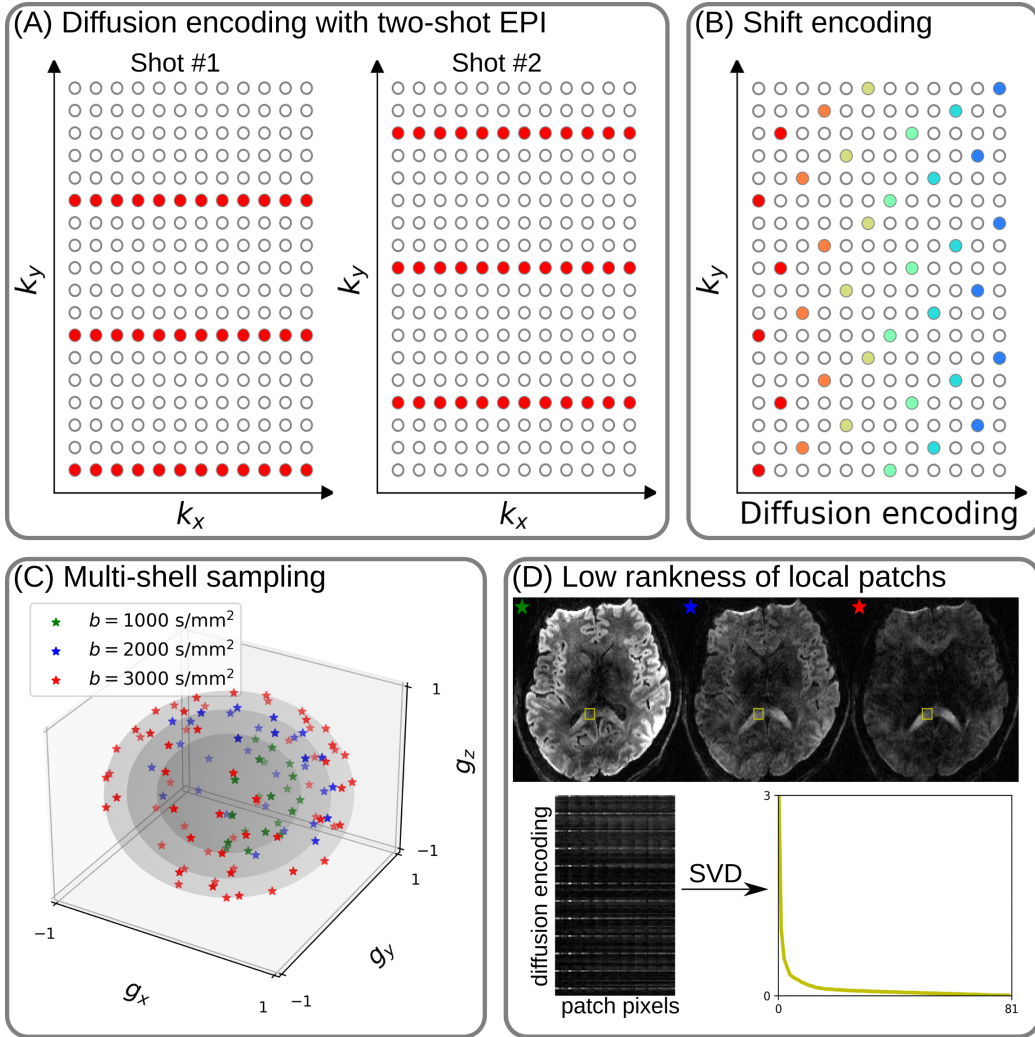


Figure 1: (A) An example DW-MRI acquisition with two-shot interleaved EPI acquisition. (B) The proposed k_y shifted diffusion encoding scheme. This example employs two shots per DW image. Therefore, every two columns have the same color. (C) An example multi-shell sampling scheme. (D) Low rankness of local image patches (as extracted from the yellow blocks) along multi-shell diffusion encoding.

134 2.3. Forward modeling

135 Our proposed acquisition method yields multi-dimensional but slice col-
136 lapsed k -space data $\mathbf{y}_{c,q,s}$, where c, q, s denotes the index of the coil sensitivity
137 map, the diffusion encoding, and the shot, respectively. Acquisition modeling
138 needs to consider several aspects.

First, the acquired k -space data \mathbf{y} is mapped from individual shot images $\mathbf{x}_{q,s,z}$ via the forward model,

$$\mathbf{y}_{c,q,s} = \mathbf{P}_{q,s} \Sigma \boldsymbol{\Theta}_z \mathbf{F} \mathbf{S}_c \mathbf{x}_{q,s,z} \quad (1)$$

$$\mathbf{y} := \mathbf{E}_1 \mathbf{x} \quad (2)$$

139 Here, the encoding matrix \mathbf{E}_1 comprises a chain of linear operators. Every
140 shot image \mathbf{x} is point-wise multiplied by a set of coil sensitivity maps (\mathbf{S}) and
141 Fourier transformed (\mathbf{F}). The output is then point-wise multiplied by the
142 multi-slice phase map ($\boldsymbol{\Theta}$) with z the slice index in simultaneously excited
143 slices. This operator shifts individual slice along the phase-encoding direction
144 via varying phase modulation (Breuer et al., 2005). The SMS k -space data
145 is then summed (collapsed, Σ) along the slice dimension and masked (point-
146 wise multiplied, \mathbf{P}) by the sampling pattern of each diffusion encoding and
147 shot.

148 Second, for diffusion MRI based on multi-shot EPI, multiple shots ac-
149 quired for a given diffusion encoding need to be combined as one DW image
150 ($\tilde{\mathbf{x}}$). A possibility is to perform magnitude average (Chen et al., 2013) or
151 root-sum-squares (RSS) (Mani et al., 2017) of shot images. This method is
152 robust to in-plane motion, but sub-optimal with respect to SNR (Guhaniyogi R3.27
153 et al., 2016). Alternatively, shot combination can be done via shot-to-shot

154 phase variation correction (Liu et al., 2005; Chen et al., 2013). This can
 155 be incorporated to our formulation as point-wise multiplication between the
 156 shot-to-shot phase variation (Φ) and the DW image ($\tilde{\mathbf{x}}$),

$$\mathbf{x}_{q,s,z} = \Phi_{q,s,z} \tilde{\mathbf{x}}_{q,z} \quad (3)$$

157 Note that $\tilde{\mathbf{x}}$ can be obtained by applying the adjoint of Φ to \mathbf{x} . In MUSE,
 158 Φ is obtained by parallel imaging reconstruction of all shots with subsequent
 159 phase smoothing of every shot image. Based on this phase correction, the
 160 complete forward model follows

$$\mathbf{y} := \mathbf{E}_2 \tilde{\mathbf{x}} = \mathbf{E}_1 \Phi \tilde{\mathbf{x}} \quad (4)$$

161 where the encoding matrix \mathbf{E}_2 comprises the chain of the shot-to-shot phase
 162 variation Φ and the encoding matrix \mathbf{E}_1 . We implemented these two encoding
 163 matrices in SigPy (Ong and Lustig, 2019).

164 *2.4. Joint k-q-slice reconstruction*

165 Based on the generalized forward models in Eqs. (2) and (4), our proposed
 166 joint *k-q*-slice reconstruction can be formulated as a three-step approach.

167 I. Joint reconstruction of all shot images by solving the following inverse
 168 problem with the LLR regularization:

$$\operatorname{argmin}_{\mathbf{x}} \|\mathbf{y} - \mathbf{E}_1 \mathbf{x}\|_2^2 + \lambda \|\mathbf{T} \mathbf{x}\|_* \quad (5)$$

169 Note that this step suffices in the case of single-shot EPI acquisition.

170 II. For multi-shot EPI acquisition, shot-to-shot phase variation is extracted
 171 from \mathbf{x} . Assuming that phase images are spatially smooth (Chen et al., R1.13

172 2013; Dai et al., 2023), only the central quarter k -space region of \mathbf{y} is
 173 used to solve for \mathbf{x} . Afterward, the reconstructed \mathbf{x} is interpolated to
 174 the full FOV. The corresponding phase is then filtered by the Hanning
 175 window.

176 III. Joint reconstruction of all DW images using the shot-combined forward
 177 model \mathbf{E}_2 with shot-to-shot phase variation from Step II:

$$\operatorname{argmin}_{\tilde{\mathbf{x}}} \|\mathbf{y} - \mathbf{E}_2 \tilde{\mathbf{x}}\|_2^2 + \lambda \|\mathbf{T} \tilde{\mathbf{x}}\|_* \quad (6)$$

178 *2.5. Locally low rank (LLR) regularization*

179 As shown in Fig. 1 (D), low rankness exists in local patches from multi-
 180 shell DW images. Intuitively, low rankness comes from the contrast variation
 181 feature of DW images. This motivates the application of LLR regularization
 182 (Trzasko and Manduca, 2011; Zhang et al., 2015) for solving the inverse
 183 problems in Eqs. (5) and (6). Here, λ is the regularization strength ($\lambda \geq 0$).
 184 \mathbf{T} represents a linear operator that firstly slides a local patch window through
 185 all DW images and then flattens every set of local patches to two-dimensional
 186 (2D) matrices. The nuclear norm regularization is enforced via singular value
 187 thresholding of all flattened 2D matrices (Cai et al., 2010). We implemented
 188 this regularization term as a proximal operator (Beck, 2017).

R3.28

189 It has been reported that LLR is prone to checkerboard artifacts when λ
 190 is too large (Hu et al., 2020). We overcome this problem by utilizing overlap-
 191 ping blocks and providing an efficient implementation. If the blocks overlap,
 192 $\mathbf{T}^H \mathbf{T}$ input \neq input, where \mathbf{T}^H denotes the Hermitian adjoint operator of R3.30
 193 \mathbf{T} . Our efficient implementation is to scale \mathbf{T}^H as $(1/\text{divisor})\mathbf{T}^H$, where the
 194 divisor matrix is obtained by $\mathbf{T}^H \mathbf{T} \mathbf{1}$. $\mathbf{1}$ denotes the matrix of ones with the
 195 same shape as the input.

R3.31

196 2.6. Reconstruction

197 The acquired raw data was read in by twixtools (<https://github.com/pehses/twixtools>). Ramp-sampling regridding and FOV/2-ghost correction were also performed in twixtools. Subsequently, coil sensitivity maps 199 were computed from reference scans using ESPIRiT (Uecker et al., 2014) in 200 SigPy (Ong and Lustig, 2019).

202 With this pre-processing as well as the implemented forward models and 203 proximal operator, both inverse problems in Eqs. (5) and (6) were solved by 204 the alternating direction method of multipliers (ADMM) (Boyd et al., 2010).

205 ADMM solves the minimization problems in an alternating update scheme,

$$\begin{cases} \mathbf{x}^{(k+1)} := \underset{\mathbf{x}}{\operatorname{argmin}} \| \mathbf{y} - \mathbf{E}(\mathbf{x}) \|^2 + \rho/2 \| \mathbf{T}\mathbf{x} - \mathbf{z}^{(k)} + \mathbf{u}^{(k)} \|_2^2 \\ \mathbf{z}^{(k+1)} := \mathcal{T}_{\lambda/\rho}(\mathbf{T}\mathbf{x}^{(k+1)} + \mathbf{u}^{(k)}) \\ \mathbf{u}^{(k+1)} := \mathbf{u}^{(k)} + \mathbf{T}\mathbf{x}^{(k+1)} - \mathbf{z}^{(k+1)} \end{cases} \quad (7)$$

206 where k denotes the ADMM iteration. \mathbf{z} is the auxiliary variable ($\mathbf{z} = \mathbf{T}\mathbf{x}$), 207 and \mathbf{u} is the Lagrangian multipliers. Importantly, when solving Eq. (2), \mathbf{x} 208 denotes shot images and \mathbf{E} denotes \mathbf{E}_1 in Eq. (7). In contrast, \mathbf{x} denotes shot- 209 combined images and \mathbf{E} denotes \mathbf{E}_2 when solving Eq. (4). \mathbf{x} can be solved 210 using linear least square algorithms, e.g. conjugate gradients (Hestenes and R3.35 Stiefel, 1952), while \mathbf{z} is updated via singular value thresholding (\mathcal{T}) with R2.8, 211 the thresholding parameter λ/ρ . The coupling parameter ρ is effective in R3.32 212 both the update of \mathbf{x} and \mathbf{z} . It acts as Tikhonov regularization strength 213 when updating \mathbf{x} , but also inversely scales the thresholding strength when 214 updating \mathbf{z} , as shown in Supporting Information Figures S1 and S2.

216 In this work, 15 ADMM iterations with $\rho = 0.05$ and $\lambda = 0.04$, and a 217 block size of 6 for LLR (refer to Supporting Information Figure S3) were

218 used. All reconstructions were done on a single A100 SXM4/NVLink GPU
219 with 40 GB memory (NVIDIA, Santa Clara, CA, USA).

R3.37

220 We compared our proposed joint reconstruction with established multi-
221 shot reconstruction techniques, specifically, MUSE (Chen et al., 2013), MUS-
222 SELS (Bilgic et al., 2019), and JULEP (Dai et al., 2023). Here, MUSE R1.3
223 and JULEP are hosted on GitHub by Dr. Dai, and MUSSELS with the
224 multi-band reconstruction feature is made available by Dr. Bilgic. Further,
225 we performed the local-PCA denoising (Manjón et al., 2013) as implemented
226 in DIPY (Garyfallidis et al., 2014) on the MUSE reconstructed DW images.

227 With reconstructed DW images, fractional anisotropy (FA) maps (Basser
228 et al., 1994) were fitted using our implementation in Python, whereas fiber
229 orientation distribution functions (fODF) (Aganj et al., 2009) were computed
230 in MITK-Diffusion (Fritzsche et al., 2012) with the spherical harmonic order
231 4 and the regularization factor 0.002. fODF maps were displayed with the
232 min-max normalization and the FA/GFA (generalized fractional anisotropy) R3.41
233 scaling factor 2.2.

234 **3. Results**

235 **3.1. Validation of the proposed two-shot EPI acquisition via retrospectively
236 undersampling from a six-shot EPI acquisition**

237 JETS reconstruction results on the six-shot prospectively fully-sampled R1.1
238 data from the acquisition protocol in Section 2.2.1, as well as on the ret-
239 retrospectively undersampled two-shot data without and with the proposed k_y
240 shift are displayed in Fig. 2. Noticeable signal loss can be observed in the 2-
241 shot reconstruction without k_y shift, as indicated by red arrows. In contrast,
242 the visible difference between the 6-shot and the k_y -shifted 2-shot reconstruc-
243 tions is smaller, especially in the averaged DW image. This is also confirmed
244 with the quantitative comparison of the normalized root mean square error
245 (NRMSE), as listed in the bottom right of difference images. The NRMSE
246 values are lower in the reconstruction with k_y shifting, indicating a closer
247 match with the 6-shot reconstruction.

248 **3.2. Three-shell diffusion acquisition at 1.0 mm isotropic resolution**

249 Results for a 1.0 mm isotropic resolution three-shell 126-direction diffu-
250 sion acquisition are show in Fig. 3. At this resolution, a severe reduction
251 of SNR can be observed for higher b -values. With such low SNR levels,
252 brain structures are completely buried below the noise level in MUSE and
253 MUSSELS. The local PCA denoiser removes noise efficiently from the recon-
254 structed MUSE images, but images from higher b -values suffer from severe
255 blurring that leads to a loss of fine image details. Only the proposed JETS
256 method with the combination of the k_y -shift encoding scheme and LLR reg-
257 ularized reconstruction allows for the resolution of brain features for higher

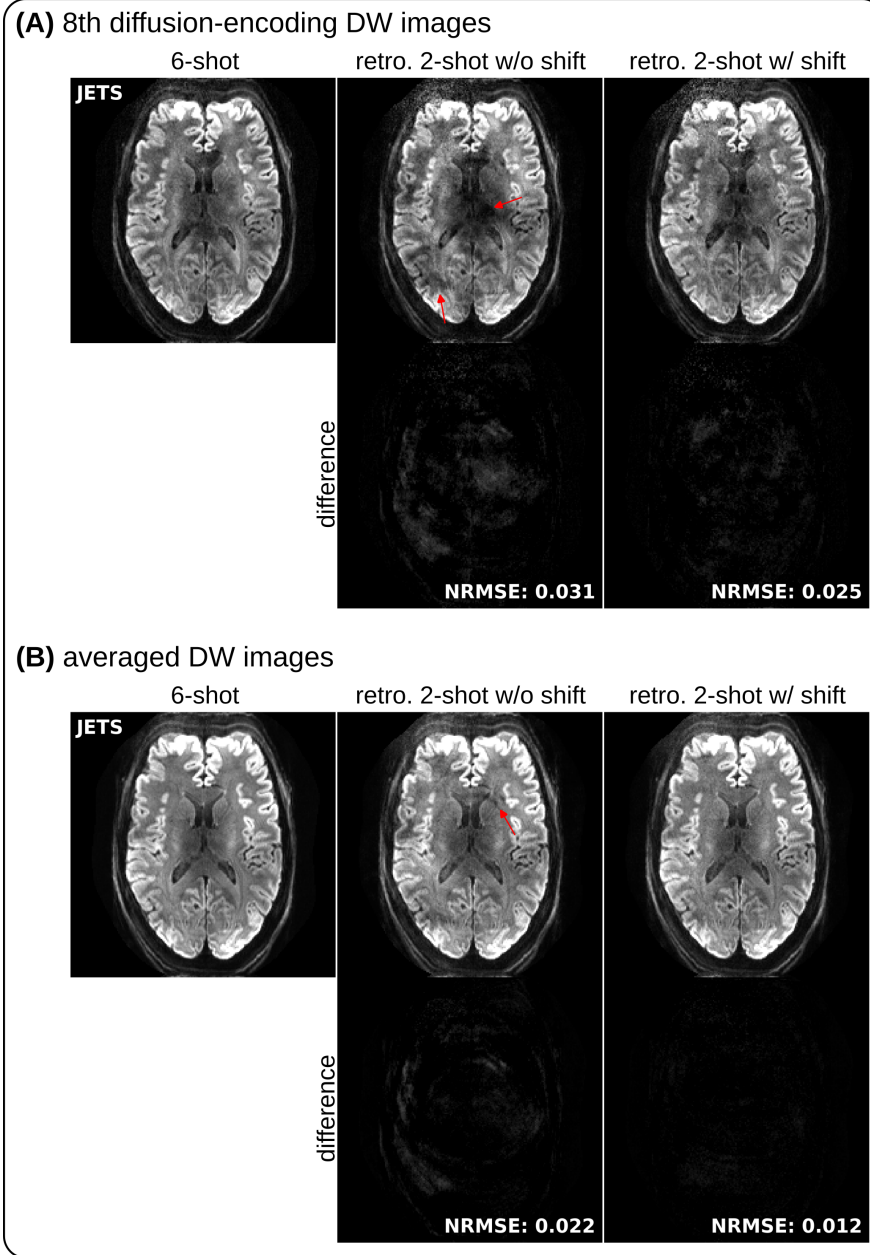


Figure 2: JETS reconstruction results on (1st column) the 6-shot sampled data from R1.1 Section 2.2.1, the retrospectively undersampled 2-shot data (2nd column) without k_y shift as well as (3rd column) with k_y shift. Difference images were obtained by subtracting the 6-shot from the 2-shot reconstructed images. (A) and (B) display the 8th DW and the averaged DW images, respectively.

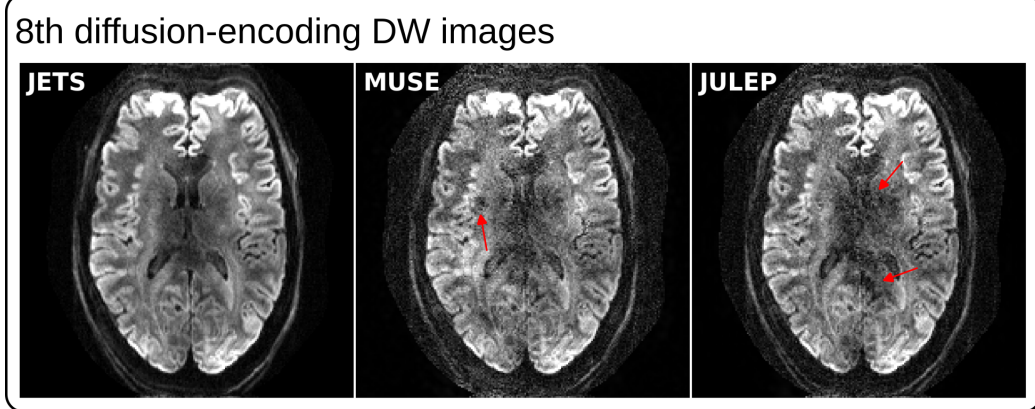


Figure 3: Comparison of reconstructed DW images on three-shell diffusion acquisition at 1 mm isotropic resolution. DW images of the 60th slice for one diffusion direction at different b -values are displayed: (left) 1000, (center) 2000, and (right) 3000 s/mm².

258 b -values.

259 Fig. 4 shows fitted FA maps in three orthogonal orientations based on
 260 the above four DW image reconstruction methods. Corresponding color-
 261 coded FA maps are provided in Supporting Information Figure S6. All FA
 262 maps are displayed with the same windowing, i.e., minimal and maximal
 263 values set as 0 and 1, respectively. The FA maps from MUSE with local
 264 PCA denoising exhibit much lower values than other methods. This may be
 265 caused by the excessive noise in DW images from MUSE or by the automatic
 266 noise estimate in the local PCA denoising algorithm (Veraart et al., 2016).
 267 Among all methods, FA maps from JETS show better quality and delineate
 268 fine details within the putamen (see white arrows).

269 Fig. 5 shows fODF maps within the rectangular regions in Fig. 4. This
 270 result again demonstrates the advantage of iterative reconstruction with LLR
 271 regularization for DW image denoising. Both MUSE and MUSSELS recon-

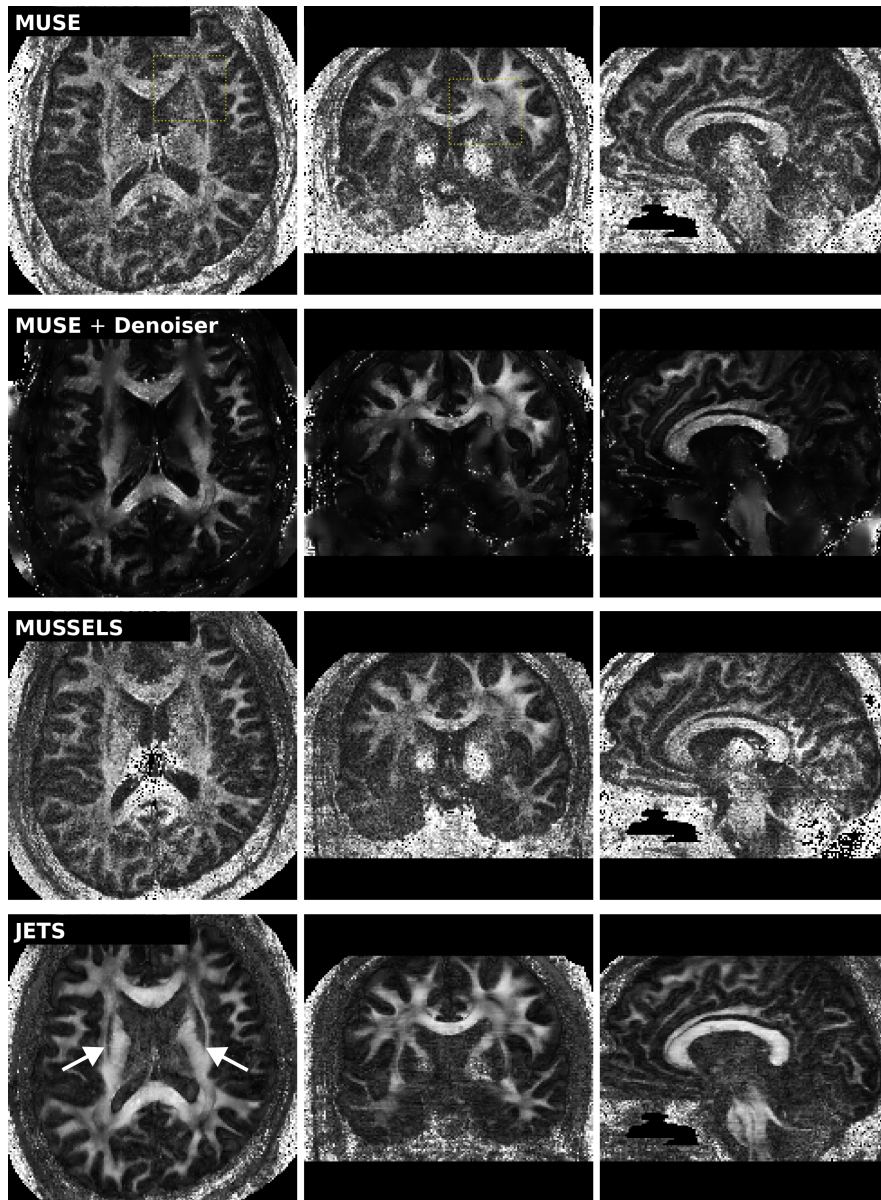


Figure 4: Comparison of reconstructed FA maps based on the 1 mm isotropic resolution three-shell diffusion acquisition. One slice from every orientation (axial, coronal, and sagittal view from left to right) was selected for display.

272 structures suffer from noise artifacts due to the use of highly accelerated
273 acquisition ($R = 8.7 \times 3$ per shot) and high b -values (up to 3000 s/mm^2). As
274 a result, their corresponding fODF maps illustrate chaotic fiber orientation.
275 With the local PCA denoiser applied to DW images reconstructed by MUSE,
276 the fODF peaks show improved smoothness, but the FA values are reduced
277 due to excessive noise in DW images. In contrast, with LLR regularization
278 applied to the spatial-diffusion patches, JETS is able to resolve crossing fibers R1.45
279 in the intersection of corpus callosum and superior longitudinal fasciculus (see
280 white arrows).

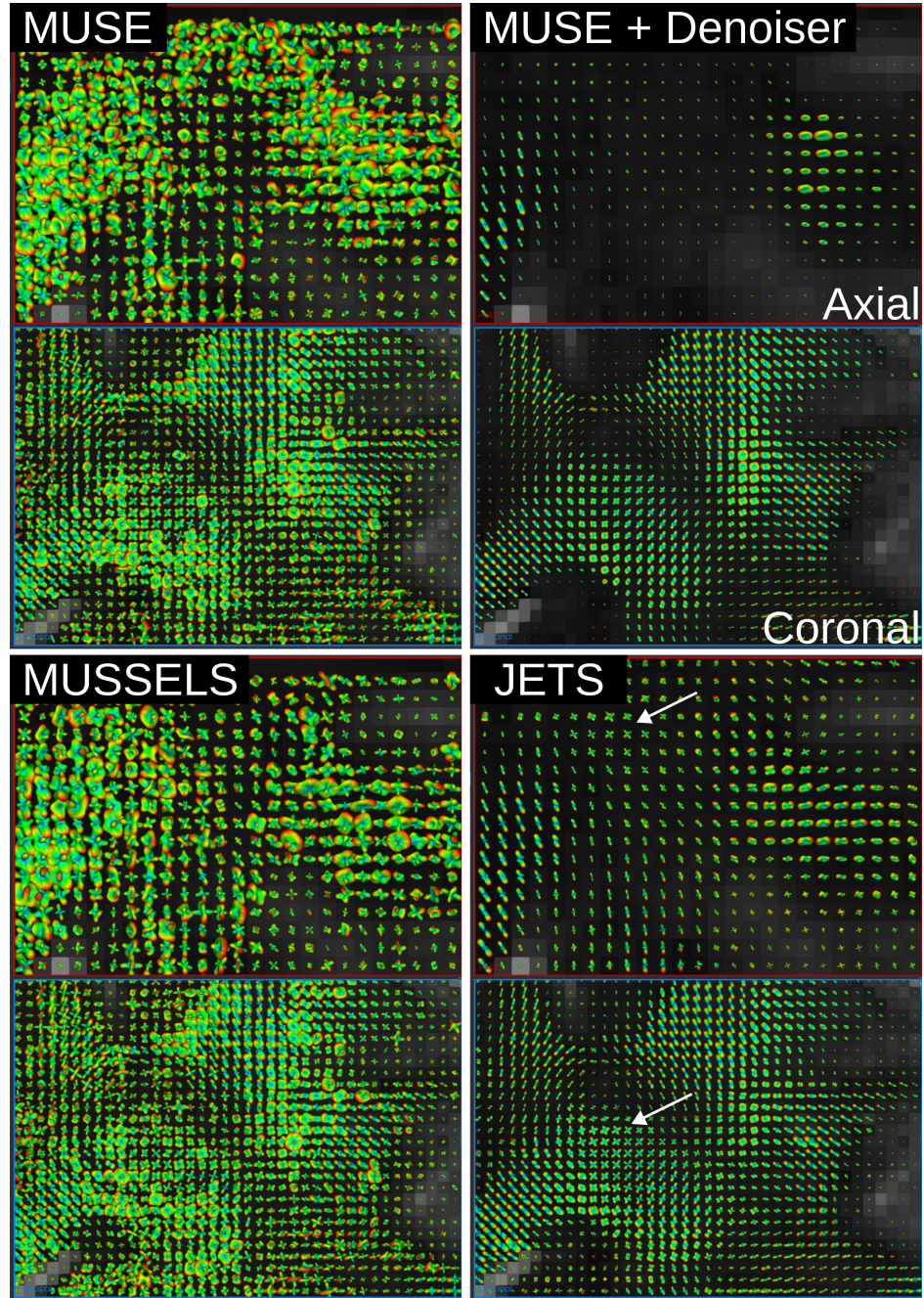


Figure 5: Comparison of fODF peaks within the dashed rectangles of (red) the axial and (blue) the coronal slices in Fig. 4, respectively.

281 **4. Discussion**

282 This work reports a novel DW-MRI technique, dubbed JETS-EPI, com- R3.45
283 prising two ingredients, multi-band k_y -shift-encoded interleaved EPI for com-
284 plementary k - q -space sampling, and a generalized joint reconstruction with
285 overlapping locally low-rank regularization to explore low rankness along the
286 diffusion encoding dimension. JETS-EPI utilizes only two shots per diffu-
287 sion-weighted image, thereby allowing for short scan times as well as high R3.46
288 spatial resolution with reduced geometric distortion. Our reconstruction uses
289 8.7×3 ($R_{\text{in-plane}} \times \text{SMS}$) fold accelerated brain DW-MRI at 7 T with 1 mm
290 isotropic resolution and 126 diffusion-direction (three shells with b -values of
291 1000, 2000, and 3000 s/mm²) in less than 23 min.

292 The reconstruction results from MUSE and MUSSELS suffer from noise
293 effects in this study, and the reasons are two-fold. First, the high in-plane
294 undersampling factor per shot hinders shot-to-shot phase variation estima-
295 tion in MUSE, whereas we proposed to jointly reconstruct all shot images
296 from the central k -space data. Further, joint reconstruction benefits from the
297 complementary k - q -space sampling, as compared to the shot-by-shot paral-
298 lel imaging reconstruction. Second, structured low-rank matrix completion
299 as used by MUSSELS usually works with at least four shots per diffusion R3.47
300 direction, whereas this study uses only two shots. The use of two shots is
301 beneficial for shorter scan time than four shots, but hinders the structured
302 low rank property in MUSSELS.

303 One limitation of JETS-EPI is the long reconstruction time due to the
304 simultaneous reconstruction of all DW images and the use of overlapping
305 locally low-rank regularization. The reconstruction of the protocols in Sec-

tion 2.2.2 and Section 2.2.3 on an A100 GPU takes about 0.5 h and 3 h per collapsed slice, respectively. To reduce the computation time, coil compression algorithms (Huang et al., 2008) can be employed to reduce the number of coils for image reconstruction. Moreover, one may deploy multi-GPU distributed computing or modern optimization algorithms (e.g. stochastic gradient descent) (Ong et al., 2020) to speed up the reconstruction.

Another limitation of JETS-EPI is the self-navigated shot-to-shot phase variation estimation, which was performed based on the central quarter k -space region of every shot. These shot k -space data is highly undersampled with $R = 8.7 \times 3$ for the 1 mm three-shell diffusion acquisition. Such high undersampling may result in sub-optimal phase estimation, especially in regions with low SNR and/or rapid phase change.

To be discussed: LLR regularization performance and reliability may degrade in the presence of motion. Also, often DWI is performed with alternating PEs for distortion correction. SNR is heterogeneous over the FOV, which may not be appropriately covered by a single regularization weight. Please, add these aspects to discussion. See also minor point 5.

Discussion on phase: Think you should add a bit more on this topic to discussion, as phase behaviour depends on several hard-to-control factors such as pulsatile motion, its impact at different locations within the brain, diffusion sensitization strength, bulk motion, ...

While this work reconstructs all DW images and then performs model fitting, an alternative approach is to directly estimate b_0 and diffusion tensors from measured k - q -space data using model-based reconstruction (Knoll et al., 2015; Dong et al., 2018; Shafieizargar et al., 2023). Compared to DW image

331 reconstruction, model-based reconstruction solves for a fewer number of un-
332 knowns, but requires strict diffusion tensor modeling and the use of nonlinear R3.49
333 least square solvers.

334 **5. Conclusions**

335 We demonstrated the JETS-EPI technique, which integrates a k_y -shifted
336 encoding interleaved EPI sequence and a joint reconstruction with overlap-
337 ping locally low-rank regularization for high spatial-angular-temporal reso-
338 lution DW-MRI at 7T. This technique requires no phase navigation, and
339 allows for high-quality DW image reconstruction with accelerated acquisi-
340 tions.

341 **Funding**

342 This work was supported by Deutsche Forschungsgemeinschaft (DFG) –
343 Project Number 513220538, as well as National Institutes of Health (NIH)
344 R01 EB024532 and P41 EB017183.

345 **Data and code available statement**

346 In the spirit of reproducible and open science, we will publish our source
347 code (<https://github.com/ZhengguoTan/sigpy>) as well as the raw k -space
348 data (<https://doi.org/10.5281/zenodo.7548595>) during the review pro-
349 cess.

350 **Acknowledgments**

351 The authors thank Dr. Peter Neher for the discussion on MITK-Diffusion.
352 The authors gratefully acknowledge the scientific support and HPC resources
353 provided by the Erlangen National High Performance Computing Center
354 (NHR@FAU) of Friedrich-Alexander-Universität Erlangen-Nürnberg (FAU)
355 under the NHR project b143dc. NHR funding is provided by federal and
356 Bavarian state authorities. NHR@FAU hardware is partially funded by the
357 German Research Foundation (DFG) – 440719683.

358 The authors thank Dr. Berkin Bilgic for making the MUSSELS source R1.2
359 code (<https://bit.ly/2QgBg9U>) publically available, Dr. Erpeng Dai for
360 sharing the JULEP source code (<https://github.com/daiep/JULEP>) on
361 GitHub, and Dr. Zhiyong Zhang for sharing the SPA-LLR source code (<https://github.com/ZZgroupSJTU/PMCmsDTI>) on GitHub.
362

363 **References**

- 364 Aganj, I., Lenglet, C., Sapiro, G., 2009. Odf reconstruction in q-ball imaging
365 with solid angle consideration, in: Proc. IEEE Int. Symp. Biomed.
366 Imaging, pp. 1398–1401. doi:[10.1109/ISBI.2009.5193327](https://doi.org/10.1109/ISBI.2009.5193327).
- 367 Andersson, J.L.R., Skare, S., Ashburner, J., 2003. How to correct suscepti-
368 bility distortions in spin-echo echo-planar images: application to diffusion
369 tensor imaging. NeuroImage 20, 870–888. doi:[10.1016/S1053-8119\(03\)00336-7](https://doi.org/10.1016/S1053-8119(03)00336-7).
- 371 Bammer, R., Keeling, S.L., Augustin, M., Pruessmann, K.P., Wolf, R., Stoll-
372 berger, R., Hartung, H.P., Fazekas, F., 2001. Improved diffusion-weighted

- 373 single-shot echo-planar imaging (EPI) in stroke using sensitivity encoding
374 (SENSE). Magn. Reson. Med. 46, 548–554. doi:[10.1002/mrm.1226](https://doi.org/10.1002/mrm.1226).
- 375 Basser, P.J., Mattiello, J., Le Bihan, D., 1994. MR diffusion tensor
376 spectroscopy and imaging. Biophys. J. 66, 259–267. doi:[10.1016/S0006-3495\(94\)80775-1](https://doi.org/10.1016/S0006-3495(94)80775-1).
- 377 Beck, A., 2017. First-order methods in optimization. Society for In-
378 dustrial and Applied Mathematics, Philadelphia, PA. doi:[10.1137/1.9781611974997](https://doi.org/10.1137/1.9781611974997).
- 380 Bilgic, B., Chatnuntawech, I., Manhard, M.K., Tian, Q., Liao, C., Iyer, S.S.,
381 Cauley, S.F., Huang, S.Y., Polimeni, J.R., Wald, L.L., Setsompop, K.,
382 2019. Highly accelerated multishot echo planar imaging through synergistic
383 machine learning and joint reconstruction. Magn. Reson. Med. 82, 1343–
384 1358. doi:[10.1002/mrm.27813](https://doi.org/10.1002/mrm.27813).
- 386 Block, K.T., Uecker, M., Frahm, J., 2007. Undersampled radial MRI with
387 multiple coils. Iterative image reconstruction using a total variation con-
388 straint. Magn. Reson. Med. 57, 1186–1098. doi:[10.1002/mrm.21236](https://doi.org/10.1002/mrm.21236).
- 389 Boyd, S., Parikh, N., Chu, E., Peleato, B., Eckstein, J., 2010. Distributed
390 optimization and statistical learning via the alternating direction method
391 of multipliers. Foundations and Trends in Machine Learning 3, 1–122.
392 doi:[10.1561/2200000016](https://doi.org/10.1561/2200000016).
- 393 Breuer, F.A., Blaimer, M., Heidemann, R.M., Mueller, M.F., Griswold, M.A.,
394 Jakob, P.M., 2005. Controlled Aliasing in Parallel Imaging Results in

- 395 Higher Acceleration (CAIPIRINHA) for Multi-Slice Imaging. Magn. Re-
396 son. Med. 53, 684–691. doi:[10.1002/mrm.20401](https://doi.org/10.1002/mrm.20401).
- 397 Butts, K., Riederer, S.J., Ehman, R.L., Thompson, R.M., Jack, C.R., 1993.
398 Interleaved echo planar imaging on a standard MRI system. Magn. Reson.
399 Med. 31, 67–72. doi:[10.1002/mrm.1910310111](https://doi.org/10.1002/mrm.1910310111).
- 400 Cai, J.F., Candès, E.J., Shen, Z., 2010. A singular value threshold-
401 ing algorithm for matrix completion. SIAM. J. Optim. 20, 1956–1982.
402 doi:[10.1137/080738970](https://doi.org/10.1137/080738970).
- 403 Chen, N.K., Guidon, A., Chang, H.C., Song, A.W., 2013. A robust multi-
404 shot scan strategy for high-resolution diffusion weighted MRI enabled by
405 multiplexed sensitivity-encoding (MUSE). NeuroImage 72, 41–47. doi:[10.1016/j.neuroimage.2013.01.038](https://doi.org/10.1016/j.neuroimage.2013.01.038).
- 407 Dai, E., Mani, M., McNab, J.A., 2023. Multi-band multi-shot diffu-
408 sion MRI reconstruction with joint usage of structured low-rank con-
409 straints and explicit phase mapping. Magn. Reson. Med. 89, 95–111.
410 doi:[10.1002/mrm.29422](https://doi.org/10.1002/mrm.29422).
- 411 Dong, Z., Dai, E., Wang, F., Zhang, Z., Ma, X., Yuan, C., Guo, H., 2018.
412 Model-based reconstruction for simultaneous multislice and parallel imag-
413 ing accelerated multishot diffusion tensor imaging. Med. Phys. 45, 3196–
414 3204. doi:[10.1002/mp.12974](https://doi.org/10.1002/mp.12974).
- 415 Fritzsch, K.H., Neher, P.F., Reicht, I., van Bruggen, T., Goch, C., Reisert,
416 M., Nolden, M., Zelzer, S., Meinzer, H.P., Stieltjes, B., 2012. MITK diffu-
417 sion imaging. Methods Inf. Med. 51, 441–448. doi:[10.3414/ME11-02-0031](https://doi.org/10.3414/ME11-02-0031).

- 418 Garyfallidis, E., Brett, M., Amirbekian, B., Rokem, A., van der Walt, S.,
419 Descoteaux, M., Nimmo-Smith, I., Contributors, D., 2014. DIPY, a library
420 for the analysis of diffusion MRI data. *Front. Neuroinform.* 8, 1–17. doi:[10.3389/fninf.2014.00008](https://doi.org/10.3389/fninf.2014.00008).
- 421
- 422 Griswold, M.A., Jakob, P.M., Heidemann, R.M., Nittka, M., Jellus, V.,
423 Wang, J., Kiefer, B., Haase, A., 2002. Generalized autocalibrating par-
424 tially parallel acquisitions (GRAPPA). *Magn. Reson. Med.* 47, 1202–1210.
425 doi:[10.1002/mrm.10171](https://doi.org/10.1002/mrm.10171).
- 426
- 427 Guhaniyogi, S., Chu, M.L., Chang, H.C., Song, A.W., Chen, N.K., 2016. Mo-
428 tion immune diffusion imaging using augmented MUSE for high-resolution
429 multi-shot EPI. *Magn. Reson. Med.* 75, 639–652. doi:[10.1002/mrm.25624](https://doi.org/10.1002/mrm.25624).
- 430
- 431 Heidemann, R.M., Porter, D.A., Anwander, A., Feiweier, T., Heberlein, K.,
432 Knösche, T.R., Turner, R., 2010. Diffusion imaging in humans at 7 T
433 using readout-segmented EPI and GRAPPA. *Magn. Reson. Med.* 64, 9–
434 14. doi:[10.1002/mrm.22480](https://doi.org/10.1002/mrm.22480).
- 435
- 436 Hestenes, M.R., Stiefel, E., 1952. Methods of conjugate gradients for solving
437 linear systems. *J. Res. Natl. Bur. Stand.* 49, 409–436. doi:[10.6028/jres.049.044](https://doi.org/10.6028/jres.049.044).
- 438
- 439 Hu, Y., Wang, X., Tian, Q., Yang, G., Daniel, B., McNab, J., Hargreaves, B.,
2020. Multi-shot diffusion-weighted MRI reconstruction with magnitude-
based spatial-angular locally low-rank regularization (SPA-LLR). *Magn.*
Reson. Med. 83, 1596–1607. doi:[10.1002/mrm.28025](https://doi.org/10.1002/mrm.28025).

- 440 Huang, F., Vijayakumar, S., Li, Y., Hertel, S., Duensing, G.R., 2008. A soft-
441 ware channel compression technique for faster reconstruction with many
442 channels. *Magn. Reson. Imaging* 26, 133–141.
- 443 Jones, D.K., 2010. Diffusion MRI: Theory, methods, and applications. Oxford
444 University Press.
- 445 Knoll, F., Raya, J.G., Halloran, R.O., Baete, S., Sigmund, E., Bammer, R.,
446 Block, T., Otazo, R., Sodickson, D.K., 2015. A model-based reconstruction
447 for undersampled radial spin-echo DTI with variational penalties on the
448 diffusion tensor. *NMR Biomed* 28, 353–366.
- 449 Le Bihan, D., Breton, E., Lallemand, D., Grenier, P., Cabanis, E., Laval-
450 Jeantet, M., 1986. MR imaging of intravoxel incoherent motions: appli-
451 cation to diffusion and perfusion in neurologic disorders. *Radiology* 161,
452 401–407. doi:[10.1148/radiology.161.2.3763909](https://doi.org/10.1148/radiology.161.2.3763909).
- 453 Liu, C., Moseley, M.E., Bammer, R., 2005. Simultaneous phase cor-
454 rection and SENSE reconstruction for navigated multi-shot DWI with
455 non-Cartesian k -space sampling. *Magn. Reson. Med.* 54, 1412–1422.
456 doi:[10.1002/mrm.20706](https://doi.org/10.1002/mrm.20706).
- 457 Lustig, M., Donoho, D., Pauly, J.M., 2007. Sparse MRI: The application of
458 compressed sensing for rapid MR imaging. *Magn. Reson. Med.* 58, 1182–
459 1195. doi:[10.1002/mrm.21391](https://doi.org/10.1002/mrm.21391).
- 460 Mani, M., Jacob, M., Kelley, D., Magnotta, V., 2017. Multi-shot sensitivity-
461 encoded diffusion data recovery using structured low-rank matrix comple-

- 462 tion (MUSSELS). Magn. Reson. Med. 78, 494–507. doi:[10.1002/mrm](https://doi.org/10.1002/mrm).
- 463 [26382](#).
- 464 Manjón, J.V., Coupé, P., Concha, L., Buades, A., Collins, D.L., Robles, M.,
465 2013. Diffusion weighted image denoising using overcomplete local PCA.
466 PLoS One 8, e73021. doi:[10.1371/journal.pone.0073021](https://doi.org/10.1371/journal.pone.0073021).
- 467 Mansfield, P., 1977. Multi-planar image formation using NMR spin echoes.
468 J Phys C 10, 55–58. doi:[10.1088/0022-3719/10/3/004](https://doi.org/10.1088/0022-3719/10/3/004).
- 469 Maudsley, A.A., 1980. Multiple-line-scanning spin density imaging. J. Magn.
470 Reson. 41, 112–126. doi:[10.1016/0022-2364\(80\)90207-3](https://doi.org/10.1016/0022-2364(80)90207-3).
- 471 Merboldt, K.D., Hanicke, W., Frahm, J., 1985. Self-diffusion NMR imag-
472 ing using stimulated echoes. J. Magn. Reson. 64, 479–486. doi:[10.1016/0022-2364\(85\)90111-8](https://doi.org/10.1016/0022-2364(85)90111-8).
- 473
- 474 Mori, S., Crain, B.J., Chacko, V.P., Van Zijl, P.C.M., 1999. Three-
475 dimensional tracking of axonal projections in the brain by mag-
476 netic resonance imaging. Ann. Neurol. 45, 265–269. doi:[10.1002/1531-8249\(199902\)45:2<265::AID-ANA21>3.0.CO;2-3](https://doi.org/10.1002/1531-8249(199902)45:2<265::AID-ANA21>3.0.CO;2-3).
- 475
- 476
- 477
- 478 Ong, F., Lustig, M., 2019. SigPy: A Python package for high performance
479 iterative reconstruction, in: Proceedings of the 27th Annual Meeting of
480 ISMRM, Montréal, CAN, p. 4819.
- 481 Ong, F., Zhu, X., Cheng, J.Y., Johnson, K.M., Larson, P.E.Z., Vasanawala,
482 S.S., Lustig, M., 2020. Extreme MRI: Large-scale volumetric dynamic
483 imaging from continuous non-gated acquisitions. Magn. Reson. Med. 84,
484 1763–1780. doi:[10.1002/mrm.28235](https://doi.org/10.1002/mrm.28235).

- 485 Pipe, J.G., Farthing, V.G., Forbes, K.P., 2002. Multishot diffusion-weighted
486 FSE using PROPELLER MRI. Magn. Reson. Med. 47, 42–52. doi:[10.1002/mrm.10014](https://doi.org/10.1002/mrm.10014).
- 488 Porter, D.A., Heidemann, R.M., 2009. High resolution diffusion-weighted
489 imaging using readout-segmented echo-planar imaging, parallel imaging
490 and a two-dimensional navigator-based reacquisition. Magn. Reson. Med.
491 62, 468–475. doi:[10.1002/mrm.22024](https://doi.org/10.1002/mrm.22024).
- 492 Pruessmann, K.P., Weiger, M., Scheidegger, M.B., Boesiger, P., 1999.
493 SENSE: Sensitivity encoding for fast MRI. Magn. Reson. Med. 42, 952–
494 962. doi:[10.1002/\(SICI\)1522-2594\(199911\)42:5<952::AID-MRM16>3.0.CO;2-S](https://doi.org/10.1002/(SICI)1522-2594(199911)42:5<952::AID-MRM16>3.0.CO;2-S).
- 496 Ra, J.B., Rim, C.Y., 1993. Fast imaging using subencoding data sets from
497 multiple detectors. Magn. Reson. Med. 30, 142–145. doi:[10.1002/mrm.1910300123](https://doi.org/10.1002/mrm.1910300123).
- 499 Roemer, P.B., Edelstein, W.A., Hayes, C.E., Souza, S.P., Mueller, O.M.,
500 1990. The NMR phased array. Magn. Reson. Med. 16, 192–225. doi:[10.1002/mrm.1910160203](https://doi.org/10.1002/mrm.1910160203).
- 502 Setsompop, K., Fan, Q., Stockmann, J., Bilgic, B., Huang, S., Cauley, S.F.,
503 Nummenmaa, A., Wang, F., Rathi, Y., Witzel, T., Wald, L.L., 2018. High-
504 resolution *in vivo* diffusion imaging of the human brain with generalized
505 slice dithered enhanced resolution: Simultaneous multislice (gSlider-SMS).
506 Magn. Reson. Med. 79, 141–151. doi:[10.1002/mrm.26653](https://doi.org/10.1002/mrm.26653).

- 507 Setsompop, K., Gagoski, B.A., Polimeni, J.R., Witzel, T., Wedeen, V.J.,
508 Wald, L.L., Adalsteinsson, E., 2012. Blipped-controlled aliasing in parallel
509 imaging for simultaneous multislice echo planar imaging with reduced g -
510 factor penalty. Magn. Reson. Med. 67, 1210–1224. doi:[10.1002/mrm](https://doi.org/10.1002/mrm).
511 [23097](#).
- 512 Shafieizargar, B., Jeurissen, B., Poot, D.H.J., Klein, S., Van Audekerke,
513 J., Verhoye, M., den Dekker, A.J., Sijbers, J., 2023. ADEPT: Accurate
514 diffusion echo-planar imaging with multi-contrast shoTs. Magn. Reson.
515 Med. 89, 396–410. doi:[10.1002/mrm.29398](https://doi.org/10.1002/mrm.29398).
- 516 Trzasko, J., Manduca, A., 2011. Local versus global low-rank promotion in
517 dynamic MRI series reconstruction, in: Proceedings of the 19th Annual
518 Meeting of ISMRM, Montréal, CAN, p. 4371.
- 519 Tuch, D.S., Reese, T.G., Wiegell, M.R., Makris, N., Belliveau, J.W., Wedeen,
520 V.J., 2002. High angular resolution diffusion imaging reveals intravoxel
521 white matter fiber heterogeneity. Magn. Reson. Med. 48, 577–582. doi:[10.1002/mrm.10268](https://doi.org/10.1002/mrm.10268).
- 523 Uecker, M., Lai, P., Murphy, M.J., Virtue, P., Elad, M., Pauly, J.M.,
524 Vasanawala, S.S., Lustig, M., 2014. ESPIRiT – an eigenvalue approach
525 to autocalibrating parallel MRI: Where SENSE meets GRAPPA. Magn.
526 Reson. Med. 71, 990–1001. doi:[10.1002/mrm.24751](https://doi.org/10.1002/mrm.24751).
- 527 Veraart, J., Novikov, D.S., Christiaens, D., Ades-aron, B., Sijbers, J., Fiere-
528 mans, E., 2016. Denoising of diffusion mri using random matrix theory.
529 NeuroImage 142, 394–406. doi:[10.1016/j.neuroimage.2016.08.016](https://doi.org/10.1016/j.neuroimage.2016.08.016).

- 530 Wu, W., Koopmans, P.J., Andersson, J.L., Miller, K.L., 2019. Diffusion
531 Acceleration with Gaussian process Estimated Reconstruction (DAGER).
532 Magn. Reson. Med. 82, 107–125. doi:[10.1002/mrm.27699](https://doi.org/10.1002/mrm.27699).
- 533 Zhang, T., Pauly, J.M., Levesque, I.R., 2015. Accelerated parameter mapping
534 with a locally low rank constraint. Magn. Reson. Med. 73, 655–661. doi:[10.1002/mrm.25161](https://doi.org/10.1002/mrm.25161).